An Ultra-High Sensitivity Optical Fiber Refractive Index Sensor Based on Plasmonic Mach-Zehnder Interferometer

Xue Zhou, Xuegang Li, Xin Yan, Xuenan Zhang, Fang Wang, Takenobu Suzuki, Yasutake Ohishi, and Tonglei Cheng

***Abstract*—An ultra-high sensitivity refractive index sensor is proposed and designed by integrating plasmonic Mach-Zehnder interferometer and the optical fiber structure together. The configuration, the numerical simulations and the performance of the proposed structure have been analyzed and discussed by the finite element method. At the working wavelength of 1.55 μm, the designed sensor is optimized to obtain the sensing sensitivity 20141.7 nm/RIU. Furthermore, it is found that with the increase of the working wavelength, the sensitivity will also increase, thus the proposed sensor has the potential to work in the near-infrared band. This sensor not only shows a high sensitivity to refractive index detection, but also is highly applicable in the detection of liquid concentration, gas concentration or temperature.**

***Index Terms*—Surface plasmon resonance, Refractive Index Sensor, Mach-Zehnder Interferometer, optical fiber.**

I. Introduction

SURFACE plasmon polaritons (SPPs) are electron density waves transmitted at metal-dielectric or metal-air interfaces [1], which have good spatial region and local field strength [2]. A pure metal plasmonic wave provides a sub-wavelength scale light guiding but with very high propagation loss [3], thus accurate engineerings are demanded in designing the plasmonic based waveguides to carefully channelize the unique features of SPPs for linear/nonlinear photonic devices [4] and sensing applications [5]. At the satisfaction of phase matching condition between SPPs and light waves, surface plasmon resonance (SPR) would be induced, drawing on which researchers have developed sensors exhibiting superior detection performance [6], [7]. The fundamental mechanism of the SPR sensors is to detect the refractive index (RI) change of the material under test, and theoretical and experimental studies show that the SPR sensors [8], [9] are highly sensitive in detecting RI change, convenient to fabricate, able to be monitored in real time and leave out the trouble of labeling. Therefore, the investigation and improvement of optical fiber-based SPR sensors has always been a research hotspot. In 2020, Zhao *et al.* [10] proposed an ultra-resolution optical salinity quantum sensor using SPR and quantum sensing principle. In the same year, Bandaru *et al.* [11] demonstrated a rapid, wash-free, dip-type plasmonic fiber optic absorbance biosensor using SPR principle and specific binding of antigens and antibodies. Huang *et al.* [12] realized for the first time the accurate measurement of copper (II) Ion (Cu^{2+}) based on an ultrasensitive localized SPR sensor. Despite the technical improvement and advantages concerning SPR sensors, there are disadvantages that cannot be ignored. For example, their working wavelengths are mostly concentrated in the visible band, which high limited the application.

Interferometer, including Michelson interferometer [13], Mach-Zehnder interferometer (MZI) [14], Sagnac interferometer [15], Fabry-Perot interferometer [16], is one of the most sensitive optical interrogation methods[17]. The principle of MZI is that the optical signal is divided into two parts and enters the reference arm and the measuring arm respectively, and then the interference occurs after the convergence at the other end. And the measured information can be obtained by the interference fringe movement. In 2019, Zhang *et al.*[18] proposed a temperature sensor based on a UV-curable polymer-infiltrated Mach–Zehnder interferometer created in a graded index fiber. Experiments show that the sensor has high refractive index sensitivity and temperature sensitivity. In 2018, Li *et al.* [19] proposed an MZI sensor based on magnetic fluid filled PCF and realized simultaneous measurement of temperature and magnetic field using interference between different modes. MZI is a kind of the well-known label free optical sensing devices,

Manuscript received May 26, 2021; revised August 4, 2021; accepted August 16, 2021. Date of publication August 20, 2021; date of current version September 3, 2021. This work was supported in part by the National Key Research and Development Program of China under Grant 2017YFA0701200, in part by the National Natural Science Foundation of China under Grant 61775032, in part by Fundamental Research Funds for the Central Universities under Grants N2104022, N180704006, N2004021, and N180408018, in part by Natural Science Foundation of Science and Technology Department of Liaoning Province under Grant 2020-BS-046, in part by JSPS KAKENHI under Grants 17K18891 and 18H01504, and in part by 111 Project under Grant B16009. *(Corresponding author: Tonglei Cheng.)*

Tonglei Cheng is with the College of Information Science and Engineering, Northeastern University, Shenyang 110819, China (e-mail: chengtonglei@ise.neu.edu.cn).

Xue Zhou, Xuegang Li, Xin Yan, Xuenan Zhang, and Fang Wang are with the State Key Laboratory of Synthetical Automation for Process Industries, College of Information Science and Engineering, Northeastern University, Shenyang 110819, China (e-mail: 1710302@stu.neu.edu.cn; lixuegang@ise.neu.edu.cn; yanxin@ise.neu.edu.cn; zhangxuenan@ise.neu.edu.cn; wangfang@ise.neu.edu.cn).

Takenobu Suzuki and Yasutake Ohishi are with the Research Center for Advanced Photon Technology, Toyota Technological Institute, Tempaku, Nagoya 468-8511, Japan (e-mail: takenobu@toyota-ti.ac.jp; ohishi@toyota-ti.ac.jp).

Digital Object Identifier 10.1109/JPHOT.2021.3106298

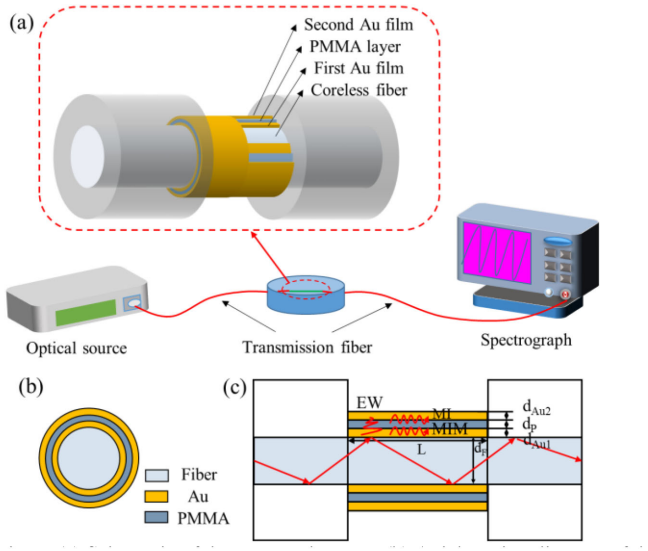

Fig. 1. (a) Schematic of the proposed sensor, (b) Axial section diagram of the proposed sensor, (c) Tangential section diagram of the proposed sensor.

which can achieve high sensitivity [20], [21] and which is not limited by the working wavelength. Recently, plasmonic MZI has been proposed [22], [23] and is believed to be promising for sensitive lable-free sensing [24], [25]. SPR sensors with different configurations, such as metal-insulator (MI), insulator-metal-insulator and metal-insulator-metal (MIM), can be used to form plasmonic MZI. However, up to now plasmonic MZI has been mainly used for on-chip sensing, using two surface plasma polarization (SPP) modes to form an MZI optical fiber sensor is a novel idea.

In this paper, we introduce a novel optical fiber plasmonic MZI sensor utilizing a MIM structure deposited on a coreless fiber to achieve dynamic RI sensing ability. In order to enhance light-matter interactions to obtain a high wavelength sensitivity to small RI change in the sensing material, the sensor parameters are optimized using the finite element method (FEM) and a sensitivity up to 20141.7 nm/RIU is achieved. To the best of our knowledge, this is the first report on optical fiber-based sensing devices drawing on plasmonic MZI to realizing highly sensitive RI detection. The proposed sensor not only has a sensitive response to RI but also exhibits an excellent ability in detecting liquid or gas concentration.

II. Theory and Design Schemes

The proposed sensor consists of the transmission optical fiber, a coreless fiber and a MIM structure, as shown in the illustration of Fig. 1(a). The transmission optical fiber adopts two commercial single-mode fibers, which are connected to the light source and the spectrometer respectively and fused at both ends of the coreless fiber to work as the input and output channel of optical signals as shown in Fig. 1(a). It is possible to fuse single-mode fiber with a specific length of coreless fiber by welding machine. After welding, magnetron sputtering machine is used to make metal film, and polymer film is made on the surface of the metal film by coating machine. The coreless fiber with a diameter of d_F serves to excite surface plasmonic wave in addition of its role as the light transmission medium. The MIM structure comprises three layers: Au film-polymethyl methacrylate (PMMA) layer-Au film. The first Au film is deposited on the coreless optical fiber with the thickness d_{Au1}, the PMMA layer coats on the first Au film with the thickness d_p and the second Au film on the PMMA layer with the thickness d_{Au2}. The length of the first Au film, the PMMA film and the second Au film is L. The surface plasma wave excited by total reflection of light on the interface of the coreless fiber and the first Au film is called MIM mode, and the one excited in the second Au film is called MI mode. These two modes propagate with propagation constant (β) and distance (L), and finally transmit out through the other transmission optical fiber while interfering with each other.

The MI mode is in direct contact with the external determinand. When the RI of the external determinand changes, the effective RI of the MI mode will change accordingly, which would in turn affect the output interference spectrum. Thus, by observing the evolution of the interference spectrum, any change in the RI of the external determinand can be monitored, realizing the sensing performance. The output signal intensity is given by [26]:

$$I_{out} = I_{MI} + I_{MIM} - 2\sqrt{I_{MI} I_{MIM}} \cos\left(\frac{2\pi L \Delta n_{eff}}{\lambda}\right) \tag{1}$$

The resonant wavelength λres and free spectrum range (FSR) are [20]:

$$\lambda_{res} = \frac{\Delta n_{eff} L}{m} \tag{2}$$

$$FSR = \frac{\lambda^2}{\Delta n_{eff} L} \tag{3}$$

where m is an integer number, $\Delta n_{eff} = n_{effMI} - n_{effMIM}$ is the difference between the MI mode and MIM mode effective indices. λ is working wavelength, I is intensity of different modes. From Eq. (1) and (2) we know that the output spectrum intensity I_{out} and resonance wavelength λ_{res} will change with the external RI difference. Thus, any change in the external RI can be detected by monitoring the output spectrum, and by detecting the change of resonance wavelength, the external RI can be measured. The sensitivity ($\Delta\lambda/\Delta$n) can be got easily from (4) [14].

$$S = \frac{\Delta\lambda}{\Delta n} = \frac{\lambda^2}{2\pi \Delta n_{eff} L \Delta n} \Delta\varphi = \frac{\lambda \Delta\left(\Delta n_{eff}\right)}{\Delta n_{eff} \Delta n} \tag{4}$$

The sensor design, optimizations, and performance analyses require an accurate mode solver, so the FEM is used by the commercial software COMSOL. First, the Physics is chosen as the Electromagnetic waves, Frequency domain. Then, the geometric structure parameters and material parameters of the model are set.

The diameter of the coreless fiber $d_F = 10$ μm is selected. The thickness of the first and second Au films is $d_{Au1} = d_{Au2} =$ 50 nm and the thickness of PMMA layer is $d_p = 160$ nm. The

RI of PMMA is calculated by the Sellmeier equation [27],

$$n(\lambda) = \sqrt{1 + \frac{1.1819\lambda^2}{\lambda^2 - 0.011313}} \tag{5}$$

where n is the RI of PMMA, λ is wavelength in μm. The dielectric constant of Au is defined by the Drude-Lorentz model [28],

$$\varepsilon_1 = \varepsilon_\infty - \frac{\omega_D^2}{\omega\left(\omega + \mathrm{j}\gamma_D\right)} - \frac{\Delta\varepsilon\Omega_L^2}{\left(\omega^2 - \Omega_\mathrm{L}^2\right) + \mathrm{j}\Gamma_L\omega} \tag{6}$$

where εm is the permittivity of Au, $\varepsilon\infty$ is the permittivity in high frequency, 5.9673 approximately. ω_D and γ_D are the plasma frequency and damping frequency, respectively. The weighting factor $\Delta\varepsilon$ is 1.09. $\omega = 2\pi c/\lambda$ is the angular frequency, where c is the velocity of light, whereas $\omega_D/2\pi = 2113.6$THz and $\gamma_D/2\pi = 15.92$THz. The frequency and spectral width of the Lorentz oscillator are Ω_L and Γ_L, respectively, $\Omega_L/2\pi = 650.07$THz and $\Gamma_L/2\pi = 104.86$THz. Transfer Matrix Method (TMM) has been used to calculate the transmission of light through the metal-insulator-metal, where n_k is the complex values of the refractive index and ε_k is the permittivity of the k^{th} layer with thickness d_k. As shown in Fig. 1(c), the designed sensor is a 5-layer structure, thus the characteristic matrix is expressed by the following equation:

$$M = \prod_{k=2}^{N} M_K = \begin{bmatrix} M_{11} & M_{12} \\ M_{21} & M_{22} \end{bmatrix}$$

$$M = \begin{bmatrix} \cos\left(\beta_k\right) & -i\sin\left(\beta_k\right)/q_k \\ -iq_k\sin\left(\beta_k\right) & \cos\left(\beta_k\right) \end{bmatrix} \tag{7}$$

where

$$\beta_k = \left(\frac{2\pi d_k}{\lambda}\right)\sqrt{\varepsilon_k - n_1^2\sin^2\theta_1}$$

$$q_k = \sqrt{\varepsilon_k - n_1^2\sin^2\theta_1}/\varepsilon_k$$

It is assumed that all the light is propagated within the fiber. If the light is having angle θ with normal interface to the fiber-metal, then the power distribution of the light is given by Eq. (8):

$$dP \propto \frac{n_1^2\sin\theta\cos\theta}{\left(1 - n_1^2\cos^2\theta\right)^2}d\theta \tag{8}$$

If the light is applied at the fiber's input and the total number of reflected rays within the sensing region (L) is $N_{ref}(\theta)$ = L/(Dtanθ) with angle θ, then the output transmitted power received at the end of the fiber can be calculated by the given formula:

$$P_{Trans} = \frac{\int_{\theta_{er}}^{\pi/2} R_P^{N_{ref}(\theta)} \frac{n_1^2\sin\theta\cos\theta}{\left(1-n_1^2\cos^2\theta\right)^2}d\theta}{\int_{\theta_{cr}}^{\pi/2} \frac{n_1^2\sin\theta\cos\theta}{\left(1-n_1^2\cos^2\theta\right)^2}d\theta} \tag{9}$$

where

$$R_P = |r_p|^2 = \frac{\left(M_{11} + M_{12}q_N\right)q_1 - \left(M_{21} + M_{22}q_N\right)}{\left(M_{11} + M_{12}q_N\right)q_1 + \left(M_{21} + M_{22}q_N\right)}$$

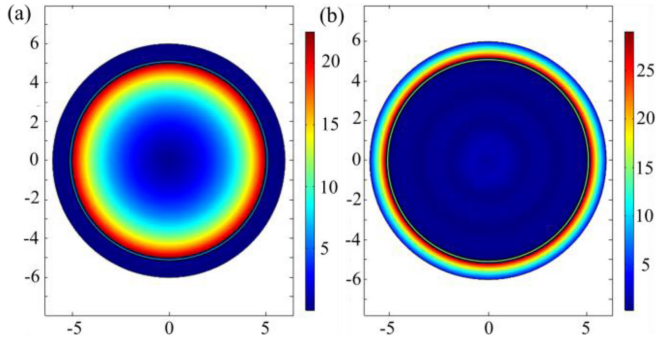

Fig. 2. Mode field distributions of (a) MIM mode, (b) MI mode.

According to Eq. (9), the reflectivity of light through the metal-insulator-metal can be obtained. A cylindrical perfect matching layer (PML) is added around the analyte and the perfect scattering boundary is set to reduce the reflection and increase the calculation accuracy. And the type of meshing is physics-controlled mesh, mesh size is normal. The mode field distributions of MIM mode and MI mode are shown Fig. 2(a) and (b), respectively. The MIM mode works as the reference arm of our proposed sensor, and from Fig. 2(a) we can see that the energy is mainly concentrated in the inner side of the first Au film. MI mode is the sensing arm of our proposed sensor. Its energy is distributed outside the second Au film and in direct contact with the external determinand, as shown in Fig. 2(b). The loss of mode can be calculated according to the Eq. (7) [29],

$$\alpha = 8.686 \times \frac{2\pi}{\lambda}\mathrm{Im}\left(n_{eff}\right) \tag{10}$$

where λ is the wavelength and Im(n_{eff}) is the imaginary part of the effective RI. The effective RIs of MIM mode and MI mode are respectively calculated at the working wavelength rang of 1520-1610 nm when the external RIs are 1.3333 (water), 1.3334, 1.3335, 1.3336 and 1.3337, as shown in Fig. 3(a). Both of the effective RIs of the two modes decrease as the wavelength increase due to the high field confinement. The MIM mode exhibits a higher effective RI, for it is in contact with the coreless fiber, while the MI mode is in contact with external determinand, and the RI of coreless fiber is higher than that of external determinand. However, with the increase of the external RI, the effective RI of MI mode increases observably, but that of the MIM mode almost shows no change. It is clear that the MI mode is more susceptible to the influence of the external environment, verifying its role as the sensing arm of the proposed sensor. Fig. 3(b) shows the calculated effective RI difference, which decreases significantly with the increase of the external RI.

As shown in Eq. (1), the length of the Au film L affects the output spectrum. And the intensity of MIM and MI modes (I_{MIM} and I_{MI}) will affect the total intensity of output but not the position of the crest or trough in the interference spectrum, so it can be considered that the intensity of these two modes will not affect the detection results. Assume that the intensities of both MIM and MI modes are 1 and fusion loss is excluded. The output spectra with different L (0.5 mm, 1 mm and 2 mm) are calculated, as shown in Fig. 4(a). It can be seen that the output

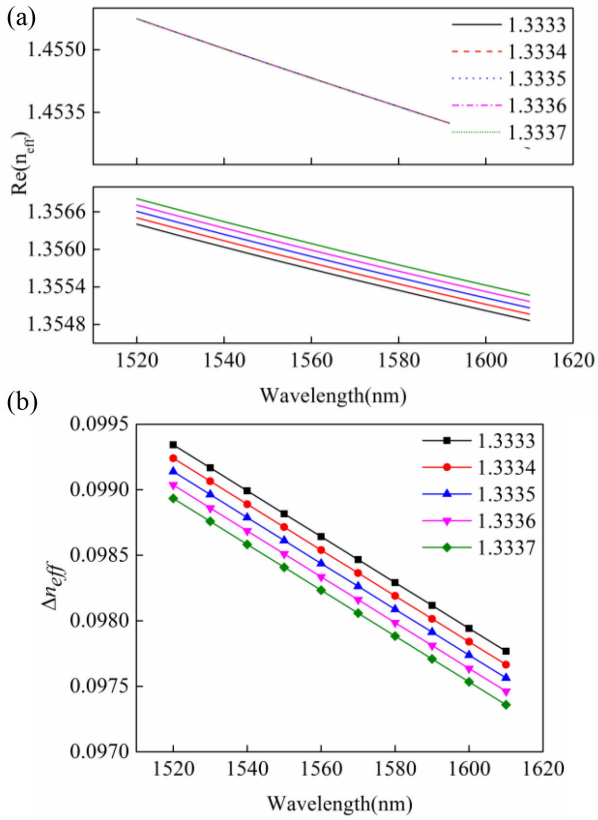

Fig. 3. (a) Effective RI of MIM and MI mode at different wavelength with different external RI, (b) Effective RI difference of MIM mode and MI mode.

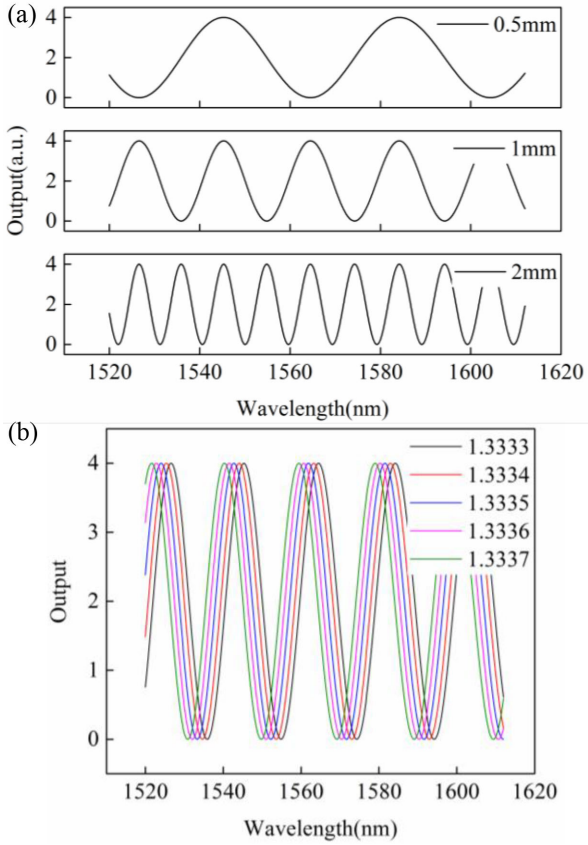

Fig. 4. (a) Output spectra with different L, L = 0.5 mm, 1 mm and 2 mm, (b) Output spectra of different external RI at L = 1 mm.

spectra are all periodic sine curves, and with the increase of L, the period of output spectrum decreases, which is consistent with Eq. (2). According to Eq. (4), the sensitivity of the proposed sensor is not affected by the length of the Au film L, so it can be considered that L does not affect the performance of the designed sensor. For the output spectrum, the smaller the full width at half maximum, the more distinguishable the crests and troughs. However, when λ_{res} shifts more than half period, it is not conducive to spectral resolution, so an appropriate L needs to be selected according to the detection range of the sensor. When L is 0.5 mm, 1 mm and 2 mm, the half period is about40nm, 20nm and 10nm, respectively. And, taking L = 1 mm as an example, the output spectra with different external RI (1.3333, 1.3334, 1.3335, 1.3336 and 1.3337) are calculated, as shown in Fig. 4(b).

With the external RI increasing, the interference spectrum moves to the short wavelength obviously. When the external RI changes by 0.0004, the resonance wavelength shifts about 8 nm. Whatever L is, the interference spectrum shifts about 8 nm with a change of 0.0004 in the external RI. For the sensors with L$\leq$0.5 mm, the half periods are $\geq$ 20 nm, much longer than 8 nm. The full width at half maximum is big, and the crests and troughs cannot be easily identified. For the sensor with L = 2 mm or longer, the half period is about 10 nm or smaller than 10 nm, which is close to 8 nm. After the spectral shift of more than half a period, the peaks and troughs cannot be resolved. Therefore, for the designed sensor, L is selected as 1 mm according to the detection RI range of 0.0004. Although the length of the metal film is short, it is not difficult to operate. After fusing a long coreless fiber with commercial single mode fiber, the fiber cutter is used to cut off the excess part so that the length of the remaining coreless fiber is 1 mm. The diameter of coreless fiber is smaller than that of single mode fiber. After coating operation, the excess metal film on the surface of single mode fiber can be easily removed without damaging the metal film on the surface of coreless fiber.

According to Eq. (4) and output spectra in Fig. 4(b), the shift of resonance wavelength ($\Delta\lambda$) with the external RI is calculated, as shown in Fig. 5. It can be seen that $\Delta\lambda$ changes linearly with the external RI. By fitting the calculated data, the relationship is obtained as follows: $\Delta\lambda$ = 21381.16-16036.27$\times$RI, and the R-Square is about 0.9999. The slope of the curve represents the sensitivity of the designed sensor, which is about 16036.27 nm/RIU, much higher than most of the existing RI sensors. In addition, the losses of MIM and MI modes under different external RI are calculated as shown in Fig. 6. The loss of MI mode is slightly larger than that of MIM mode, and both losses are hardly affected by external RI.

III. Optimization of Sensor Parameters

The sensitivity of a sensor is the ratio of the output variation to the input variation under stable working conditions. Taking the designed sensor as an example, assuming that the RI variation

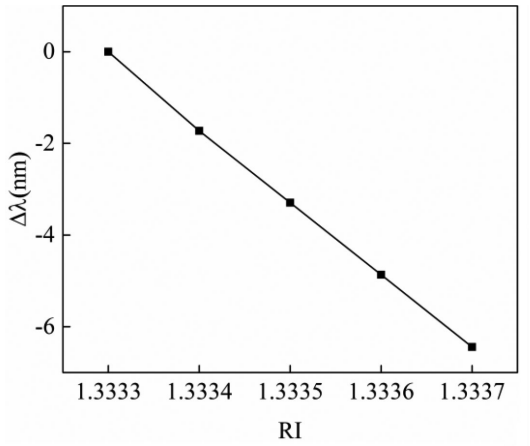

Fig. 5. Fitting curve of resonance wavelength shift and the external RI.

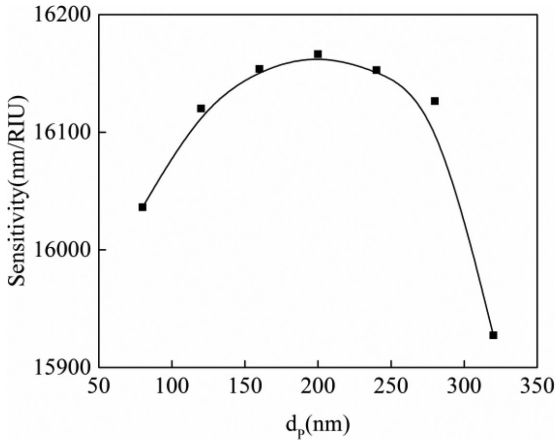

Fig. 7. Sensor's sensitivity for different PMMA layer thickness.

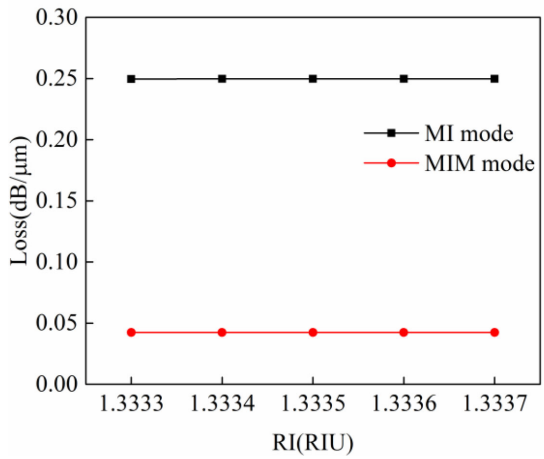

Fig. 6. Fitting curve of loss and the external RI.

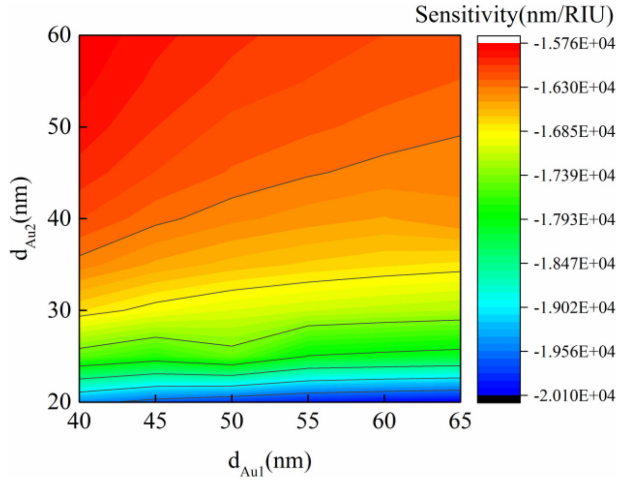

Fig. 8. Sensor's sensitivity for different Au films thickness.

of Δn and the output spectrum movement of $\Delta\lambda$, the ratio of the two is the sensitivity. The greater the sensitivity is, the higher the measurement accuracy can be obtained. But the higher the sensitivity, the narrower the measurement range. Subsequent optimizations are done based on sensors that is giving better sensitivity. In order to get better sensing performance, optimization of the sensor's structure parameters has been carried out. During the sensor design, a high RI layer is to be introduced above the first Au film to facilitate the coupling of the mode field to the second Au film, and PMMA is adopted considering its simple coating process, good light transmittance and high RI. However, this PMMA layer should be optimized regarding its thickness, for if too thin, the mode field cannot be well enhanced to couple to the second Au film; if too thick, the mode field will be restricted within the PMMA layer, and no sensing can be realized. We calculate the sensor's sensitivity with different PMMA layer thickness (d_P = 80, 120, 160, 200, 240, 280, 320 nm) at the work wavelength of 1.55 μm, as shown in Fig. 7. At d_p = 200 nm, the highest sensitivity 16176.28 nm/RIU is achieved. Therefore, the PMMA layer is optimized to be 200 nm in thickness.

The Au films as the metal layer are the key to generate plasmonic waves, and their thicknesses would naturally affect the sensitivity of the proposed sensor. With the increase of the thickness of the first Au film d_{Au1}, MIM mode can be enhanced. However, if d_{Au1} is too thick, the evanescent field cannot penetrate the first metal layer, and MI mode cannot be excited. On the other hand, a thin second Au film d_{Au2} would enhance the MI mode's perception of external RI change, but it would be too difficult to make and easy to damage if d_{Au2} goes too thin. As a result, the sensitivity of the designed sensor is calculated at the work wavelength of 1.55 μm with d_{Au1} ranging from 40 nm to 60nm and d_{Au2} from 20 nm to 60 nm, as shown in Fig. 8. The x-coordinate represents d_{Au1}, the y-coordinate represents d_{Au2}, and the histogram on the right indicates the sensitivity. It is to be noted that the greater the d_{Au1} and the smaller the d_{Au2}, the higher the sensitivity of the sensor. At d_{Au1} = 60 nm, d_{Au2} = 20 nm, the sensitivity of the designed sensor achieves 20141.7 nm/RIU.

The diameter of coreless fiber also has a certain influence on the transmission signal of the designed sensor. Thus based on the parameters already obtained from the above optimization,

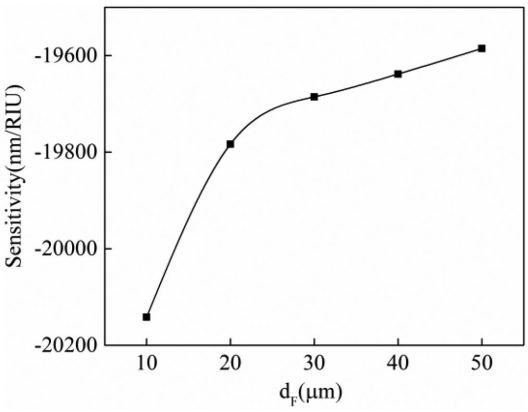

Fig. 9. Sensor's sensitivity for different coreless fiber diameter.

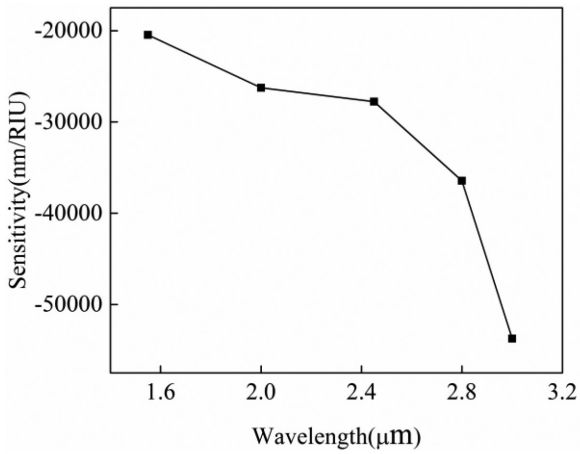

Fig. 10. Sensor's sensitivity for different work wavelength.

sensitivities at different coreless fiber diameters, $d_F = 10$, 20, 30, 40 and 50 μm are calculated, as shown in Fig. 9. With the increase of coreless fiber diameter, the wavelength sensitivity of the sensor decreases slightly. Compared with other fiber structures, the size of coreless fiber is easier to control and more choices can be made in practical applications.

The previous formula analysis shows that the working wavelength λ will also affect the sensitivity of the designed sensor. Thus based on the parameters already obtained from the above optimization, sensitivities at $\lambda = 1.55$ 2, 2.4, 2.8 and 3 μm are calculated, as shown in Fig. 10. It can be found that the longer the working wavelength, the higher the sensitivity. At $\lambda = 3$ μm, $d_F = 10$ μm, $d_P = 200$ nm, $d_{Au1} = 65$ nm, $d_{Au2} = 20$ nm and $L = 1$ mm, the highest sensitivity of the proposed sensor is achieved, which is 53730.07 nm/RIU. For the proposed sensor structure, the transmission optical fiber only serves as the input/ output channel of optical signals, so the single-mode fiber can be replaced by other fiber structures, such as multi-mode fiber. Heavy metals such as silver or copper can also be used to excite the SPR depending on the practical necessity. PMMA can be replaced by other high RI polymer materials with good light transmittance, for example, Polydimethylsiloxane (PDMS). Moreover, if optical fibers supporting transmission at longer wavelength band, such as soft glass fibers, are selected as the transmission medium, the resulted sensor structure may work in the middle infrared band and even realize the detection of gas concentration. At the present scenario, the plasmonic MZI sensor is designed based on a coreless fiber, any size of which is conveniently available in the market. The coreless fiber can be easily fused to the single-mode optical fiber using a fusion machine, the Au film can be coated by magnetron sputtering technique and the PMMA layer can be implemented using a coating machine.

IV. Conclusion

In conclusion, we proposed and designed an ultra-high sensitivity RI sensor based on plasmonic MZI. The configuration, the numerical simulation and the performance of the proposed sensor structure have been analyzed and discussed using FEM. After optimization, the designed sensor obtained the maximum wavelength sensitivity $S = 20141.7$ nm/RIU with $d_F = 10$ μm, $d_{Au1} = 65$ nm, $d_{Au2} = 20$ nm, $d_{PMMA} = 200$ nm and $L = 1$ mm at the working wavelength of 1.55 μm. The proposed sensor is small in size, simple in structure, easy to make, label-free and able dynamic detection. The designed sensor shows a great potential to be employed as a refractometer to measure temperature, liquid concentration, gas concentration, and so on.

Acknowledgement

The authors thank the anonymous reviewers for their valuable suggestions. The authors thank Liao Ning Revitalization Talents Program.

References

[1] L. B. William, D. Alain, and W. E. Thomas, "Surface plasmon subwavelength optics," *Nature*, vol. 424, no. 6950, pp. 824–830, 2003.
[2] S. Ghosh and B. M. A. Rahman, "A compact Mach–Zehnder interferometer using composite plasmonic waveguide for ethanol vapor sensing," *J. Lightw. Technol.*, vol. 35, no. 14, pp. 3003–3011, 2017.
[3] A. V. Krasavin and A. V. Zayats, "Silicon-based plasmonic waveguides," *Opt. Exp.*, vol. 18, no. 11, pp. 11791–11799, 2010.
[4] F. F. Lu *et al.*, "Surface plasmon polariton enhanced by optical parametric amplification in nonlinear hybrid waveguide," *Opt. Exp.*, vol. 19, no. 4, pp. 2858–2850, 2011.
[5] Y. Zhao, R. J. Tong, F. Xia, and Y. Peng, "Current status of optical fiber biosensor based on surface plasmon resonance," *Biosens Bioelectron*, vol. 142, no. 12, pp. 111505, Oct.–Jan. 2019.
[6] C. Caucheteur, T. Guo, and J. Albert, "Review of plasmonic fiber optic biochemical sensors: Improving the limit of detection," *Anal Bioanal Chem*, vol. 407, no. 14, pp. 3883–3897, May 2015.
[7] S. A. Maragheh, B. Olyaeefar, and R. Kheradmand, "Ultrafast nano-scale optical switching in a plasmonic interferometer with enhanced tunability," *Plasmonics*, vol. 15, no. 2, pp. 435–439, 2019.
[8] Q. Wang and B. Wang, "Sensitivity enhanced SPR immunosensor based on graphene oxide and SPA co-modified photonic crystal fiber," *Opt. Laser Technol.*, vol. 107, pp. 210–215, 2018.
[9] X. Zhou, X. Li, S. Li, G.-W. An, and T. Cheng, "Magnetic field sensing based on SPR optical fiber sensor interacting with magnetic fluid," *IEEE Trans. Instrum. Meas.*, vol. 68, no. 1, pp. 234–239, Jan. 2019.
[10] Y. Zhao, Y. Peng, X. Hu, F. Xia, and Q. Zhao, "Beating the shot-noise limit with optical fiber quantum sensors for salinity measurement," *Sensors Actuators B: Chem.*, vol. 320, no. 1-2, 2020, Art. no. 128353.
[11] R. Bandaru *et al.*, "U-bent fiber optic plasmonic biosensor platform for ultrasensitive analyte detection," *Sensors Actuators B: Chem.*, vol. 321, 2020, Art. no. 128463.

[12] Q. Huang *et al.*, "Optical fiber plasmonic sensor for the ultrasensitive detection of copper (II) ion based on trimetallic Au@agpt core-shell nanospheres," *Sensors Actuators B: Chem.*, vol. 321, 2020, Art. no. 128480.

[13] L. Li *et al.*, "High stability michelson refractometer based on an in-fiber interferometer followed with a Faraday rotator mirror," *Sensors Actuators B: Chem.*, vol. 234, pp. 674–679, 2016.

[14] X. Li, L. V. Nguyen, M. Becker, D. Pham, H. Ebendorff-Heidepriem, and S. C. Warren-Smith, "Simultaneous measurement of temperature and refractive index using an exposed core microstructured optical fiber," *IEEE J. Sel. Topics Quantum Electron.*, vol. 26, no. 4, pp. 1–7, Jul.–Aug. 2020.

[15] X. Li, L. V. Nguyen, Z. Yong, H. Ebendorff-Heidepriem, and S. C. Warren-Smith, "High-sensitivity Sagnac-interferometer biosensor based on exposed core microstructured optical fiber," *Sensors Actuators B Chem.*, vol. 269, pp. 103–109, 2018.

[16] X. Liu, M. Jiang, Q. Sui, X. Geng, and F. Song, "HCPCF-based in-line fiber Fabry-Perot refractometer and high sensitivity signal processing method," *Photonic Sensors*, vol. 7, no. 4, pp. 336–344, 2017.

[17] B. Du, J. He, M. Yang, Y. Wang, and Y. Wang, "Highly sensitive hydrogen sensor based on in-fiber Mach-Zehnder interferometer with polymer infiltration and Pt-loaded WO coating," *Opt. Exp.*, vol. 29, no. 3, pp. 4147–4158, 2021.

[18] F. Zhang *et al.*, "Highly sensitive temperature sensor based on a polymer-infiltrated Mach-Zehnder interferometer created in graded index fiber," *Opt. Lett.*, vol. 44, no. 10, pp. 2466–2469, 2019.

[19] X. Li, X. Zhou, Y. Zhao, and R.-Q. Lv, "Multi-modes interferometer for magnetic field and temperature measurement using photonic crystal fiber filled with magnetic fluid," *Opt. Fiber Technol.*, vol. 41, pp. 1–6, 2018.

[20] R. S. El Shamy, D. Khalil, and M. A. Swillam, "Mid infrared optical gas sensor using plasmonic Mach-Zehnder interferometer," *Sci Rep*, vol. 10, no. 1, pp. 1293, Jan. 28 2020.

[21] Y. Ma *et al.*, "Mach–Zehnder interferometer-based integrated terahertz temperature sensor," *IEEE J. Sel. Topics Quantum Electron.*, vol. 23, no. 4, pp. 1–7, Jul./Aug. 2017.

[22] H. Hu, X. Zeng, D. Ji, L. Zhu, and Q. Gan, "Efficient end-fire coupling of surface plasmons on flat metal surfaces for improved plasmonic Mach-Zehnder interferometer," *J. Appl. Phys.*, vol. 113, no. 5, pp. 1044–1054, 2013.

[23] S. Kamada, T. Okamoto, S. E. El-Zohary, and M. Haraguchi, "Design optimization and fabrication of Mach-Zehnder interferometer based on MIM plasmonic waveguides," *Opt Exp.*, vol. 24, no. 15, pp. 16224–16231, Jul. 2016.

[24] S. Ghosh and B. M. A. Rahman, "Design of on-chip hybrid plasmonic Mach-Zehnder interferometer for temperature and concentration detection of chemical solution," *Sensors Actuators B: Chem.*, vol. 279, pp. 490–502, 2019.

[25] O. Emre *et al.*, "Label-free and dynamic detection of biomolecular interactions for high-throughput microarray applications," *Proc. Nat. Acad. Sci. United States Amer.*, vol. 105, no. 23, pp. 7988–7992, 2008.

[26] X. Zeng, Y. Gao, H. Hu, D. Ji, Q. Gan, and F. Bartoli, "A metal-insulator-metal plasmonic Mach-Zehnder interferometer array for multiplexed sensing," *J. Appl. Phys.*, vol. 113, no. 13, 2013, Art. no. 133102.

[27] *Optical constants of (C5H8O2)n (Poly(methyl methacrylate), PMMA)*. [Online]. Available: https://refractiveindex.info/?shelf=organic&book=poly(methyl_methacrylate)&page=Sultanova

[28] A. A. Rifat, G. A. Mahdiraji, Y. M. Sua, and Y. G. Shee, "Surface plasmon resonance photonic crystal fiber biosensor: A practical sensing approach," *IEEE Photon. Technol. Lett.*, vol. 27, no. 15, pp. 1628–1631, Aug. 2015.

[29] X. Zhou, T. Cheng, S. Li, T. Suzuki, and Y. Ohishi, "Practical sensing approach based on surface plasmon resonance in a photonic crystal fiber," *OSA Continuum*, vol. 1, no. 4, pp. 1332–1340, 2018.